

Laminar boundary layer instability noise

By M. Sanjose, S. Moreau[†], A. Towne AND S. K. Lele

A direct numerical simulation is performed of the flow field around a modern controlled-diffusion airfoil within an anechoic wind-tunnel at 5° incidence and a high Reynolds number of 1.5×10^5 . The simulation compares favorably with experimental measurements of wall pressure, wake statistics, and far-field sound. In particular, the simulation captures experimentally observed high-amplitude acoustic tones that rise above a broadband hump. Both noise components are related to breathing from a recirculation bubble formed around 65-70% of the chord, and to Kelvin-Helmholtz instabilities in the separated shear layer that yield rollers that break down into turbulent vortices whose diffraction at the trailing edge produces a dipole acoustic field. A linear stability analysis of the mean flow field around the airfoil identifies convective instability in the aft portion of the airfoil where this shedding occurs for frequencies covering the broadband hump, and also provides estimates of the tonal frequencies.

1. Introduction

Airfoil self-noise can be seen as the canonical aeroacoustic problem for wall-bounded flows and directly relates to the minimum noise generated by a fixed wing or a rotating machine. This phenomenon is caused by the scattering of boundary-layer vortical disturbances into acoustic waves at the airfoil trailing edge. It has been extensively studied both experimentally and numerically, essentially focusing on the turbulent flow regime over the airfoil (8° geometrical incidence) (Roger & Moreau 2004; Wang *et al.* 2009; Sanjose *et al.* 2011). However, as Christophe *et al.* (2015) pointed out, a slight decrease of incidence yielded a flow bifurcation and a significant change of the suction-side boundary layer. Padois *et al.* (2016) stressed that such a flow change could also yield a significant noise increase with the appearance of sharp tones over a broadband hump. Indeed, tonal noise has been observed on several airfoils for various flow regimes (Probsting *et al.* 2014). This noise is particularly strong and relevant at low to transitional Reynolds numbers, typical of drones or UAV applications, yet no consensus has been reached on its origin. Another open question is whether the broadband hump and the tones are caused by an aeroacoustic or hydrodynamic feedback.

In this study, a three-dimensional compressible Direct Numerical Simulation (DNS) accounting for the full open-jet wind-tunnel setup with a jet width of 0.5 m is performed at an incidence of 5° and a high Reynolds number based on the chord length of 1.5×10^5 for which a significant tonal noise on a broadband hump is experimentally observed. The challenges of such a simulation compared to previous simulations (Desquesnes *et al.* 2007; Jones *et al.* 2008) are the high-Reynolds number transitional flow with possibly large flow separations, and the effect of the wind-tunnel jet. In Section 2, the formulation and computational setup are outlined. Section 3 is devoted to the aerodynamic results. Section 4 studies the noise sources and the far-field acoustic propagation. Section 5

[†] Université de Sherbrooke, Canada

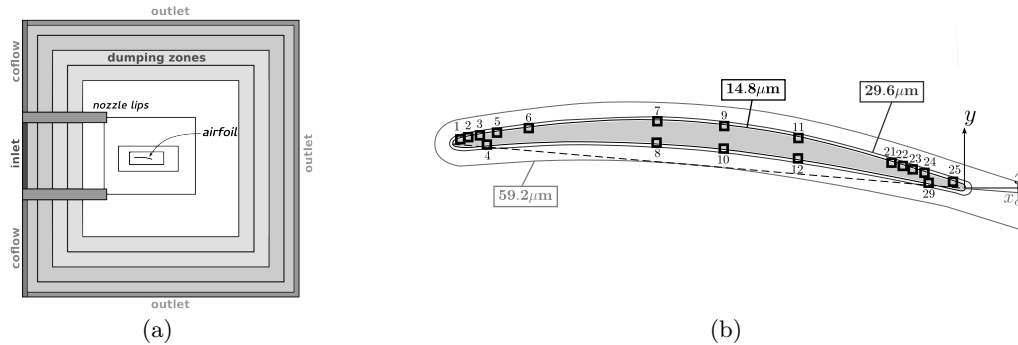


FIGURE 1. Sketch of the numerical setup with highlight of the refinement zone. (a) Numerical setup. (b) Refinement around the airfoil.

contains a linear stability analysis that provides some original insight into the noise mechanisms. Finally, conclusions are drawn in Section 6.

2. Numerical setup

Similarly to the attached boundary-layer case on the CD airfoil at 8° (Sanjose *et al.* 2011), the direct numerical simulation is performed using the Lattice Boltzmann Method rather than with the classical Navier-Stokes equation to proceed faster in time. This choice is even more justified in the present case as the observed unsteadiness of the acoustic and consequently flow field may require more through-flow times $t^* = tU_\infty/C$ than previously (t is time, $C = 13.56$ cm the chord length and $U_\infty = 16$ m/s the free stream velocity), and installation effects from the wind-tunnel may play an important role (Moreau *et al.* 2003). The Lattice Boltzmann Method (LBM) solves the mesoscopic kinetic equations, i.e., the Boltzmann equation for a set of particle density functions with a collision source term, to predict macroscopic fluid dynamics. This set of equations recovers the compressible Navier-Stokes equations in the limit of low Mach numbers, i.e. $M < 0.5$. All present simulations have been obtained with the commercial code Powerflow 5.1 from EXA Corporation in DNS mode.

To avoid using a hybrid method as in previous incompressible Large Eddy Simulation (LES) studies (Wang *et al.* 2009; Christophe *et al.* 2015), the computational domain involves a thin slice of the corresponding full anechoic wind-tunnel, as described by Sanjose *et al.* (2011). The grid spanwise extension has been limited to 12% of the chord length because of the restriction on the current LBM to cubic voxels. As the present simulation involves the same Reynolds number as the reference case, the same grid topology is used around the CD profile with zones of Volume Refinement (VR) of similar size that insured dimensionless distance to the wall y^+ below 1. The three-dimensional grid has about 640 millions voxels with ten levels of consecutive grid refinements, as shown in Figure 1. Absorbing VRs (shown in gray in Figure 1) are set around the simulation box in which the laminar viscosity is gradually increased to mitigate the acoustic waves and avoid their reflection back in the computational domain. More details on the numerical setup are provided by Sanjose *et al.* (2011). The initial condition for the simulation was taken from a preliminary simulation on a coarser grid with the first two finer VRs removed. The refined simulation initially contained a laminar recirculation bubble at the leading edge that migrated to the final third of the airfoil after about six through-flow times, as

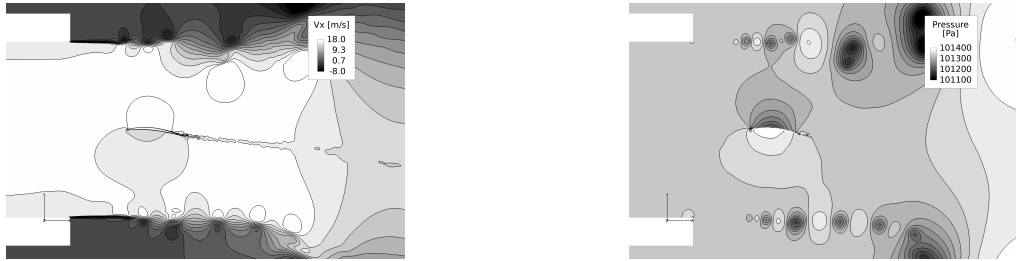


FIGURE 2. DNS instantaneous result in the full wind-tunnel setup: velocity contours (left) and pressure contours (right).

previously observed by Christophe *et al.* (2015) in their LES at 6° . This led to a total transient period of about 10 through-flow times.

3. Aerodynamic results

3.1. Overall flow topology

The overall flow topology in the whole wind-tunnel setup is shown in Figure 2. In these instantaneous flow fields, the turbulent airfoil wake and the jet deflection by the airfoil can be clearly seen. The jet is initially laminar and undergoes vortex pairing and transition to turbulence above the trailing edge of the airfoil. This is far enough downstream not to induce any modification of incidence as recently observed on high-lift devices. Moreover, including the jet effect in the simulation yields the proper airfoil loading as shown below, and also the direct noise propagation to the far field.

To gain more insight into the flow unsteadiness in the whole domain, four characteristic time-traces of the wall pressure fluctuations are shown in Figure 3. As mentioned above, in all probes the transient regime (hashed zone) corresponds to the first 10 flow-through times with the burst at $t^* = 6$ corresponding to the migration of the laminar recirculation bubble from the leading edge (as in the 8° case) to close to the trailing edge. At RMP#5, a smooth laminar pressure signal is observed. Only a large, damped smooth oscillation can be seen, which is also present in the other probes. This corresponds to a large overall pressure oscillation in the whole wind-tunnel, which should be discarded in all signals. Similar time-traces are obtained up to RMP#11, which shows intermittent bursts in its signal, sign of transition to turbulence. These bursts are more and more amplified toward the trailing edge as evidenced in RMP#21. In the latter time-trace, alternative regions of calmer and more intense fluctuations can be clearly seen, which justified the following detailed post-processing on the windows shown as five gray bands in Figure 3. Small volumes of the complete flow field are then saved around the airfoil for each window in addition to the wall pressure field.

To qualitatively assess the differences in flow fields between the two sets of events, isosurfaces of the second invariant of the velocity gradient, the Q factor, are shown for the first two windows in Figure 4 for the same constant value of Q . For both windows, the boundary layer is laminar and no vortical structures can be seen up to mid-chord. After mid-chord, natural instabilities grows in the laminar boundary layer as Tollmien-Schlichting waves (small ripples on the airfoil surface) that die out when the flow separates (at about 70% chord length). The separated shear layer then becomes unstable, and this Kelvin-Helmholtz (K-H) instability yields rollers. This initial two-dimensional shear-layer roll-up is then followed by a significant three-dimensional distortion and break-up of the

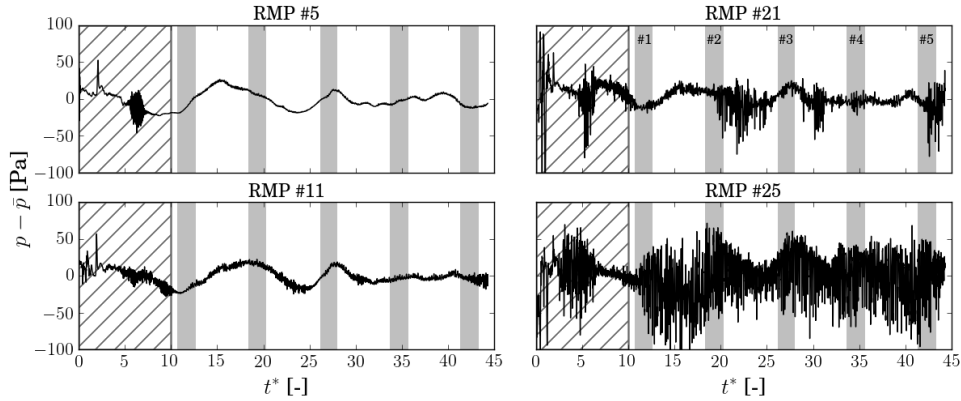


FIGURE 3. Time trace of DNS wall pressure fluctuations at different RMPs.

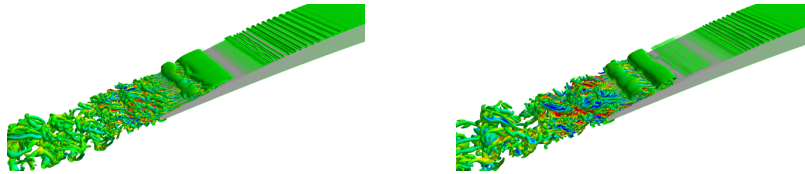


FIGURE 4. Q-criterion: Window 1 (left) and Window 2 (right).

coherent vortices. Such a process has been described in detail for several laminar recirculation bubbles by Marxen & Henningson (2011) and Jones *et al.* (2008), for instance. In the present case, the strength and size of the rollers vary with the event. In the first window (calm event), the 2D roller is thin and long, yielding smaller vortices when it breaks up. In the second window (intense event), the roller is thicker and shorter, yielding larger and more intense vortices in the transition process. Such a strong variation of the vortex strength and consequently of the boundary-layer thickness is also seen in the high-resolution Particle Image Velocimetry (PIV) measurements that have been performed in a parallel experiment.

3.2. Boundary-layer analysis

The above events described above can be quantitatively assessed using the various boundary-layer parameters on the airfoil. Figure 5 shows (a) the mean wall pressure coefficient C_p , (b) the mean friction coefficient on the airfoil C_f , and the mean boundary-layer shape factor H . The averages have been computed for the five windows shown in Figure 3. The mean airfoil loading is similar to the previous LES computation at 6° , showing signs of flow separation after mid-chord (Christophe *et al.* 2015). Significant variations are observed between the different events, the most intense of which compares very well with the C_p measurements. The friction coefficient confirms the flow separation in the aft portion of the airfoil at all times. Yet, the calm events of windows 1, 3 and 4 yield longer recirculation bubbles between 75% and 95% of chord, whereas the bursting events (windows 2 and 5) yield shorter bubbles between 65% and 85% of chord, with a slight reattachment followed by a second flow separation and a final reattachment before the trailing edge (stronger vortex shedding). This finding shows that the recirculation bubble is not only breathing with time but also triggering some vortex shedding. This shedding is further confirmed by looking at the shape factor along the airfoil. Below 70%

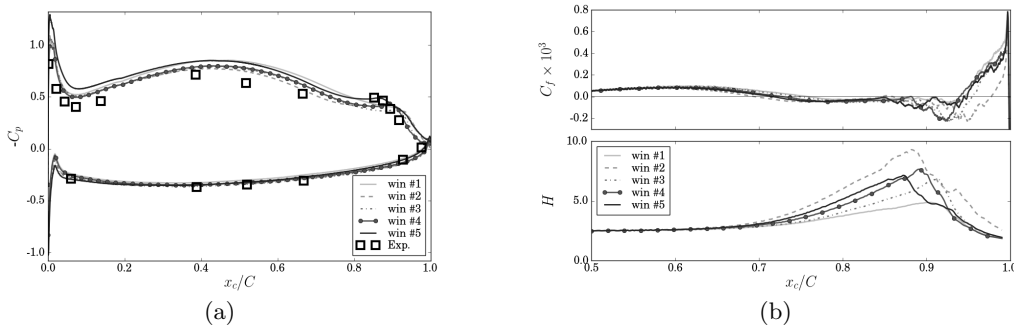


FIGURE 5. Boundary layer parameters. (a) Mean pressure coefficient. (b) Mean friction (top) and boundary layer shape (bottom) coefficients.

of the chord the shape factor H along the suction side is around 2.4, typical of a laminar boundary layer. It drastically increases to a maximum where the C_f is minimum. Flow separation occurs when $H \simeq 3.5$. Close to the trailing edge the shape factor goes below 2.4, typical of the limit of turbulent flow separation and finally settles around 1.8, typical of a turbulent boundary layer. The latter variation explains the critical change in the pressure fluctuations from RMP #21 to RMP #25 shown in Figure 3: the boundary layer tends to transition and reattach just before the trailing edge. The strong variations of the boundary-layer parameters on the five windows further emphasize the unsteady behavior of the recirculation.

3.3. Wake analysis

To assess the quality of the DNS even more closely, the wake evolution is compared in Figure 6 with PIV measurements at several locations downstream of the trailing edge. The wake statistics are again performed in the time windows shown in Figure 3. As highlighted by the wall pressure time-traces in Figure 3, the boundary layer on the suction side is quite unstable and yields noticeably different wake developments, as shown in Figure 4. On the one hand, in windows 2 and 5, large vortices are shed from the recirculation bubble yielding wider and deeper mean wake profiles that match the PIV measurements very well for both velocity components (Figure 6). Similarly, stronger and more asymmetric turbulence is produced during these events, with turbulent intensity comparing well with experiment (Figure 6, right). On the other hand, windows 1, 3 and 4 exhibit thinner wakes with shallower velocity deficits. The turbulence level on the suction side is also lower than in the PIV measurements. The latter are therefore dominated by the bursting events.

Moreover, the current mesh density (Figure 1) allows resolving the turbulent kinetic energy spectra to be resolved up to the Kolmogorov scale in the whole turbulent region: the final 15% chord length from the trailing edge and the wake. For instance, the energy spectra scaled by the Kolmogorov scale η_K and the velocity scale u_η , computed from the laminar viscosity and the turbulent dissipation, is shown in Figure 7(a) for a probe located inside the wake. The spectra shape shows in particular the scale separation with quite large inertial subrange with the typical $-5/3$ slope and a significant energy content up to the Kolmogorov scale. For large scales, modulation from the boundary layer instability appears as humps which participate in the energy production as they reasonably align with the typical $+2$ slope.

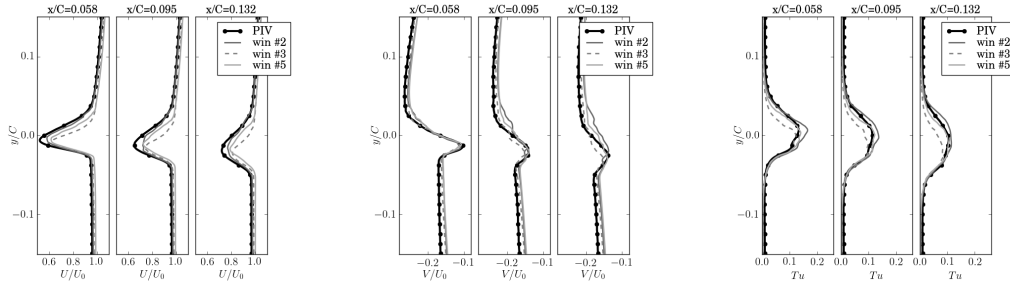


FIGURE 6. Mean velocity components and turbulence intensity in the wake.

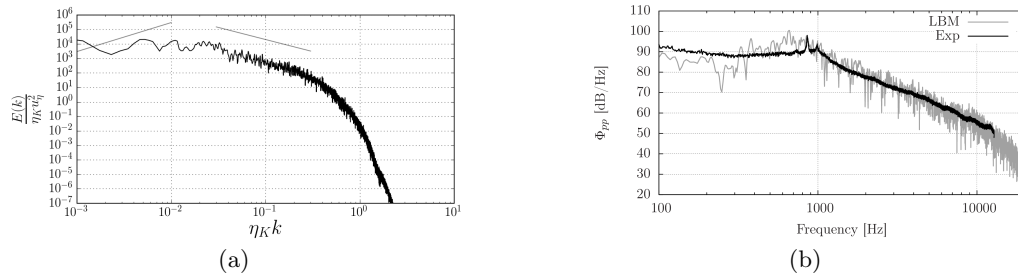


FIGURE 7. DNS turbulent spectra in the near wake and on the airfoil close to the trailing edge. (a) Turbulent energy spectra normalized by the Kolmogorov scales at $x/C=0.132$ and $y/C=0.007$. (b) PSD of wall pressure fluctuations at RMP#24.

3.4. Dynamic mode decomposition of the DNS flow field

For further insight, a frequency analysis is performed by applying the Dynamic Mode Decomposition (DMD) to a set of instantaneous flow fields (Schmid 2010). Since DMD is memory consuming, the decomposition is performed in the volume recorded during the above five windows with the signal including the three velocity components and pressure. Two separate decompositions are performed: one for velocity and one for pressure, both using 248 snapshots from window 2, corresponding to the more intense fluctuations that seem to dominate the PIV measurements. Figure 8 (a) first shows the corresponding scaled spectra. The velocity shows two maxima, one at low frequency corresponding to the recirculation bubble breathing, and a second one at 694 Hz that corresponds to the most intense fluctuations in the flow domain. Two additional peaks are seen at 387 and 1044 Hz. Similarly, the pressure spectra have three main peaks, a main one at 691 Hz and two secondary ones at 398 and 1049 Hz. These dominating frequencies during this bursting period are summarized in Table 1. The velocity and pressure modes corresponding to the common main peak are shown in Figure 8 (b) and highlight the K-H instability and consequent vortex shedding described above.

4. Acoustic results

4.1. Wall-pressure fluctuations

According to Curle's acoustic analogy, for an airfoil at such a low Mach number, the actual noise sources are the wall pressure fluctuations. Wall pressure spectra are then computed at all probes shown in Figure 1(b). These spectra converge after 22 flow-through times. They all show a broadband hump between 300 and 1200 Hz with several small tones

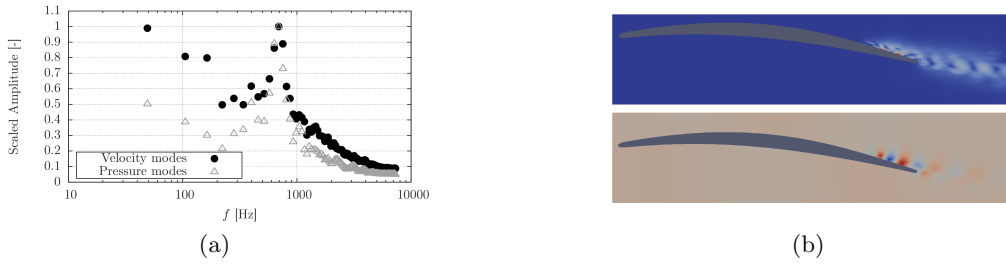


FIGURE 8. DMD analysis results obtained on window #2. (a) Scaled DMD spectra. (b) Velocity (top) and pressure (bottom) main DMD mode at about 690 Hz.

Far-field (exp.)	wall p (exp.)	DMD (U)	DMD (p)	FWH	wall p (DNS)	LST
579		387	398	544	550	391
737		694	691	670	670	703
864	860			781-860	840	
991	1000	1044	1049	990	1000	1012

TABLE 1. Tones found in all experimental, numerical and theoretical analyses.

on top, as shown in Figure 7(b). On the suction side, all spectra up to RMP#11 are dominated by this spectral feature, with a sharp roll-off at high frequencies typical of a laminar boundary layer. For RMP#11, a significant broadband hump centered at about 3000 Hz and two harmonics appear. Transition to turbulence then occurs and subsequent probes close to the trailing edge from RMP#21 to #25 show typical fuller turbulent spectral decay, as shown in Figure 7(b). Excellent agreement is seen for the broadband levels and spectral shapes. Tones are also seen as in the measurement but with more peaks that can also be broader. These tones are also reported in Table 1.

4.2. Far-field acoustic pressure

The radiated acoustic field is first shown in Figure 9 (left) by the iso-contours of the dilatation field. The overall field in the full computational domain clearly shows the dipolar nature of the radiated noise and clarifies that the main noise mechanism is the diffraction at the trailing edge. Some reflection can be observed at the end point of the nozzle lips. The diffraction by the shear layers is also found to be negligible, as expected at this low Mach number. The radiated acoustic field is dominated by mid-frequencies (large wavelengths corresponding to about 1 kHz and larger). This field could be related to the tones seen in the noise spectra measured 1.3 m perpendicular to the airfoil at midspan on both pressure and suction sides (Figure 9, left). The corresponding DNS spectra are computed from the wall pressure fluctuations on the airfoil with the Ffowcs Williams and Hawkins analogy. Good spectral shape and sound levels are obtained compared to measurements. Higher tones are, however, found below 800 Hz and broadband humps extend to 2000 Hz.

5. Linear stability analysis

Some of the spectral properties of the flow are now related to linear instabilities of the mean flow computed in window 2. Since the mean flow is varying slowly along the

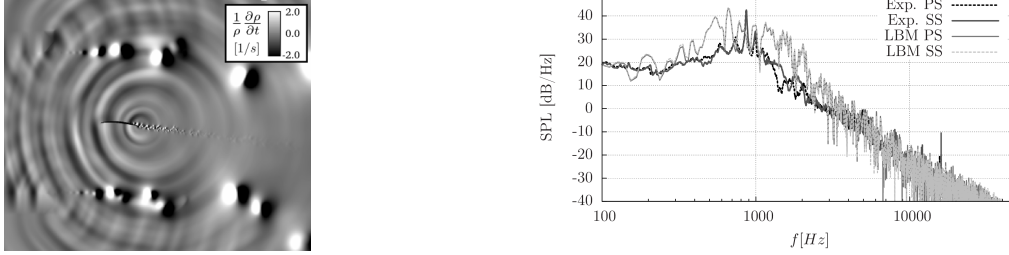


FIGURE 9. Dilatation field (left) and acoustic spectra (right).

airfoil, it is valid to perform a local stability analysis at each value of the curvilinear coordinate ξ that varies from 0 to 1 from the leading edge to the trailing edge along the suction side of the airfoil. Accordingly, the fluctuations are assumed to take the form of two-dimensional traveling-waves, $q'(\xi, \eta, t) = \hat{q}(\eta) e^{i\alpha\xi - i\omega t}$. Inserting this ansatz into the linearized Navier-Stokes equations, applying some additional simplification afforded by the properties of the flow, and numerically discretizing the equations in the η -direction normal to the airfoil lead to an equation at each ξ of the form

$$[-i\omega\mathbf{I} + i\alpha\mathbf{A} + \mathbf{B}]\hat{\mathbf{q}} = 0. \quad (5.1)$$

Solutions satisfying Eq. (5.1) exist only for certain combinations of ω and α , which define the local modes of the flow.

5.1. Absolute stability analysis

One potential source of the observed tones would be the presence of an intrinsic oscillation related to absolute instability of Kelvin-Helmholtz on the re-circulation bubble (Rodríguez *et al.* 2013). Within the weakly non-parallel analysis, absolute instabilities are described by modes that satisfy Eq. (5.1) as well as the zero-group-velocity condition.

$$\frac{\partial\omega}{\partial\alpha} = 0. \quad (5.2)$$

A mode (ω^0, α^0) satisfying these conditions is said to be absolutely unstable if $\omega_i^0 > 0$. In this case, the mode will grow at its source leading to an intrinsic oscillation that is capable of producing a discrete tone at the frequency ω_r^0 . The subscripts r and i indicate the real and imaginary parts, respectively. Modes that satisfy Eqs. (5.1) and (5.2) correspond to saddle-points in the complex α -plane and cusps in the complex ω -plane. In this work, ω^0 is computed by locating cusps using a grid of complex α -values.

The absolute growth-rate ω_i^0 of the Kelvin-Helmholtz mode is shown in Figure 10(a) as a function of chord-wise position ξ along the suction side of the airfoil. Since it is negative everywhere, the Kelvin-Helmholtz waves are not absolutely unstable. Also shown is the maximum value of ω_i taken over all real-values of α . Since this value is positive (over the latter part of the airfoil) but ω_i^0 is negative, the Kelvin-Helmholtz waves are convectively unstable (CU) in this region. The re-circulation bubble is absolutely stable (S) but convectively unstable (CU), which can be explained by the low level of the reverse flow of -2 m/s (12% of the mean incoming velocity).

5.2. Spatial stability analysis

The spatial growth of periodic disturbances is next studied by finding solutions of Eq. (5.1) for real values of ω . The maximum value of α_i is plotted as a function of ξ

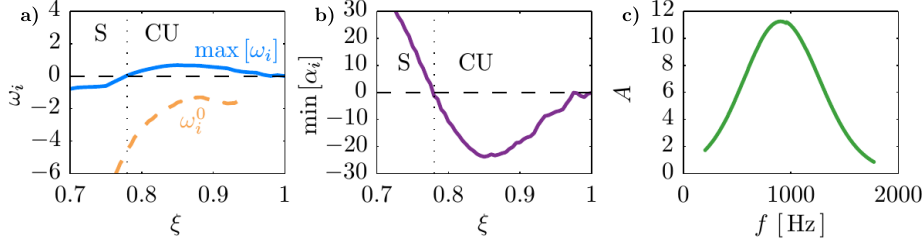


FIGURE 10. Kelvin-Helmholtz instability of the re-circulation bubble: (a) maximum temporal growth-rate and absolute growth rate; (b) maximum spatial growth-rate; (c) amplification factor.

in Figure 10(b). The cumulative amplification of the Kelvin-Helmholtz waves as they convect down the airfoil can be measured by the amplification factor

$$A(\omega) = \exp\left(-\int_{\xi_0}^1 \alpha_i(\omega, \xi) d\xi\right). \quad (5.3)$$

Here, ξ_0 is the (frequency dependent) location where the Kelvin-Helmholtz wave first becomes unstable. The amplification factor is plotted in Figure 10(c). The broad peak centered at 900 Hz matches well with the broad hump observed in the near- and far-field PSD. This confirms that the Kelvin-Helmholtz wave, rather than Tollmien-Schlichting waves, constitutes the dominant instability mechanism leading an acoustic response in this flow.

Using the model proposed by Kingan & Pearse (2009), the eigenvalues obtained from the spatial stability analysis can also be used to obtain a crude estimate of the tonal frequencies. The hypothesis underpinning this model is that the tones are produced by a feedback loop between growing downstream-propagating instability waves and upstream-propagating acoustic waves. These waves reinforce each other only if the total phase change over the loop, which is given by the expression

$$\Phi(\omega) = \int_{\xi_0}^1 \alpha_r(\omega, \xi) d\xi + \pi + \frac{\omega}{1-M}, \quad (5.4)$$

equals an integer multiple of 2π . This model predicts the appearance of tones at 391, 703, 1012, and 1332 Hz shown in Table 1. While some of these values seem to match tones observed in the data others do not, whereas the model contains several uncertainties that could lead to discrepancies. A global stability approach should allow more precise predictions of the tonal frequencies in future.

6. Conclusions

Airfoil tonal noise generation has been studied at a high Reynolds number based on the chord length of 1.5×10^5 , using direct numerical simulation of the flow and acoustic field with a Lattice Boltzmann Method. A geometrical angle-of-attack with respect to the nozzle axis of 5° has been selected as it experimentally showed a persistent tone (Padois *et al.* 2016). The numerical results compare favorably with the experimental database: mean loading and wall pressure fluctuations with Remote Microphone Probes, wake statistics with high-resolution PIV and far-field acoustic measurements. The same persistent tonal noise over a broadband hump with strong amplitude modulation of the tones is obtained. The tone and its modulation are related to breathing from a recirculation bubble formed around 65-70% of the chord, and to Kelvin-Helmholtz instabilities in

the separated shear layer that yield rollers that break down into turbulent vortices. The latter diffract at the airfoil trailing edge and produce the dipole acoustic field. The linear stability analysis of the mean flow field around the airfoil yields convective instability for frequencies covering the broadband hump, in the aft portion of the airfoil where this shedding occurs.

Acknowledgments

The authors thank V. Moureau, P. Schmid for their kind collaborations during the Summer Program. A. Mann and F. Perot from EXA Corp. are gratefully acknowledged. Computations were made on the supercomputer Mammoth-MP2 from Université de Sherbrooke, managed by Calcul Québec and Compute Canada. The experiments were performed by P. Jaiswal, PhD student at Université de Sherbrooke.

REFERENCES

- CHRISTOPHE, J., MOREAU, S., HAMMAN, C.W., WITTEVEEN, J.A.S. & IACCARINO, G. 2015 Uncertainty quantification for the trailing edge noise of a controlled-diffusion airfoil. *AIAA J.* **53**, 42–54.
- DESQUESNES, G., TERRACOL, M. & SAGAUT, P. 2007 Numerical investigation of the tone noise mechanism over laminar airfoils. *J. Fluid Mech.* **591**, 155–182.
- JONES, L.E., SANDBERG, R.D. & SANDHAM, N.D. 2008 Direct numerical simulations of forced and unforced separation bubbles on an airfoil at incidence. *J. Fluid Mech.* **602**, 175–207.
- KINGAN, M. & PEARSE, J. 2009 Laminar boundary layer instability noise produced by an aerofoil. *J. Sound Vib.* **322**, 808–828.
- MARXEN, O. & HENNINGSON, D.S. 2011 The effect of small-amplitude convective disturbances on the size and bursting of a laminar separation bubble. *J. Fluid Mech.* **671**, 1–33.
- MOREAU, S., HENNER, M., IACCARINO, G., WANG, M. & ROGER, M. 2003 Analysis of flow conditions in free-jet experiments for studying airfoil self-noise. *AIAA J.* **41**, 1895–1905.
- PADOIS, T., LAFFAY, P., IDIER, A. & MOREAU, S. 2016 Tonal noise of a controlled-diffusion airfoil at low angle of attack and Reynolds number. *J. Acoust. Soc. Am.* **140**, EL113–EL118.
- PROBSTING, S., SERPIERI, J. & SCARANO, F. 2014 Experimental investigation of aerofoil tonal noise generation. *J. Fluid Mech.* **747**, 656–687.
- ROGER, M. & MOREAU, S. 2004 Trailing edge noise measurements and prediction for a subsonic loaded fan blade. *AIAA J.* **42**, 536–544.
- RODRÍGUEZ, D., GENNARO, E. & JUNIPER, M. 2013 The two classes of primary modal instability in laminar separation bubbles. *J. Fluid Mech.* **734**, R4, doi:10.1017/jfm.2013.504.
- SANJOSE, M., MOREAU, S., KIM, M.S. & PEROT, F. 2011 Aerodynamic noise of a two-dimensional wing with high-lift devices. *AIAA Paper 2011-2716*, 17th AIAA/CEAS Aeroacoustics Conference, Portland, Oregon.
- SCHMID, P.J. 2010 Dynamic mode decomposition of numerical and experimental data. *J. Fluid Mech.* **656**, 5–28.
- WANG, M., MOREAU, S., IACCARINO, G. & ROGER, M. 2009 LES prediction of wall pressure fluctuations and noise of a low-speed airfoil. *Int. J. Aeroacoust.* **8**, 177–197.